Journal of Statistical Physics, Vol. 107, Nos. 1/2, April 2002 (© 2002)

Simulations of Water Flow Through Bordered Pits of Conifer Xylem

A. Valli,[1–3] A. Koponen,[2] T. Vesala,[1] and J. Timonen [2]

Received February 14, 2001; accepted June 8, 2001

Bordered pits between tracheids play an important role in the water conductivity of conifer xylem. There have been many attempts to model xylem as a water conducting medium, and to estimate its permeability. As the microscopic structure of xylem is highly complex, it is however very difficult to numerically solve the flow equations. New methods have recently been developed by which the flow is simulated rather than found by solving appropriate equations. In this work the lattice-Boltzmann method was used to simulate the flow in bordered pits of conifer xylem, and their permeability was thereby determined. To this end the permeability of two-dimensional screens was also analyzed.

KEY WORDS: Lattice-Boltzmann method; conifer xylem; tracheid; bordered pit.

1. INTRODUCTION

Water flow from the soil through plants to the atmosphere is one of the most important factors in the biosphere-atmosphere interactions. This process involves several physical, chemical and biological aspects which interact with each other (see, e.g., ref. 1), and form a highly complex system. Wood (xylem) is cellular in structure. A typical cellular structure of *Pinus radiata* is displayed in Fig. 1. The fluid conducting part of the xylem consists of tracheids, which are hollow cells, the inner parts (lumens) of which have been emptied of organic material. These lumens, together with

[1] Department of Physics, P.O. Box 64, FIN-00014 University of Helsinki, Finland; e-mail: valli@pcu.helsinki.fi

[2] Department of Physics, University of Jyväskylä, P.O. Box 35, FIN-40351 Jyväskylä, Finland.

[3] Helsinki Polytechnic, Bulevardi 31, FIN-00180 Helsinki, Finland.

0022-4715/02/0400-0121/0 © 2002 Plenum Publishing Corporation

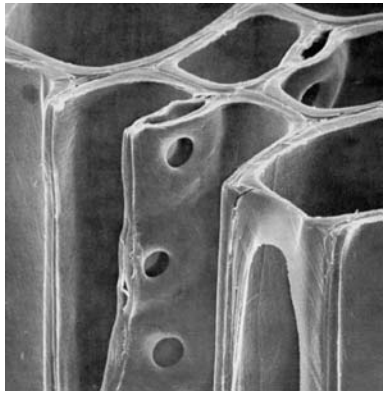

Fig. 1. A system of tracheids that belongs to the water conducting part of the xylem (*Pinus radiata L.*). Bordered pits are visible on tracheid walls. Courtesy of the Kluwer Academic Publishers.[30]

the openings (pits) connecting them, form a porous network, which enables the flow of water (sap) trough the tissue.

This article will be restricted to the flow of sap through a pit connecting two neighboring tracheids. The dynamics of the flow is rather complicated due to the complex geometry of the pit, which includes a margo that suspends the central impermeable part, the torus (Fig. 2). The margo consists of a loose mesh of fibrils through which the sap can pass (Fig. 3). Numerical simulation of flow through the margo is thus a demanding task. However, bordered pits make a big contribution to the hydraulic resistance of xylem, and detailed studies of the related fluid dynamics are therefore well motivated, especially as direct experimental information is very difficult to obtain (see, e.g., ref. 2). When the flow through pits is understood, simulations of flow through a tracheid, and the xylem composed of them, can sensibly be performed. Based on these simulations, the large-scale hydraulic resistance of trees, for which experimental results are available for comparison, can be estimated. Finally, all understanding gained in this way will be valuable when the sap flow of an entire living tree is modeled, or field experiments on e.g., diurnal variations in the stem diameter, embolism or transpiration are interpreted.

This work utilizes the lattice-Boltzmann method,[3–6] which is a relatively new approach in computational fluid dynamics. It originated from the lattice-gas model[7, 8] and has mesoscopic characteristics as opposed to the methods based on a numerical solution of the Navier–Stokes equation. It has been successfully applied to many "difficult" flow problems, which

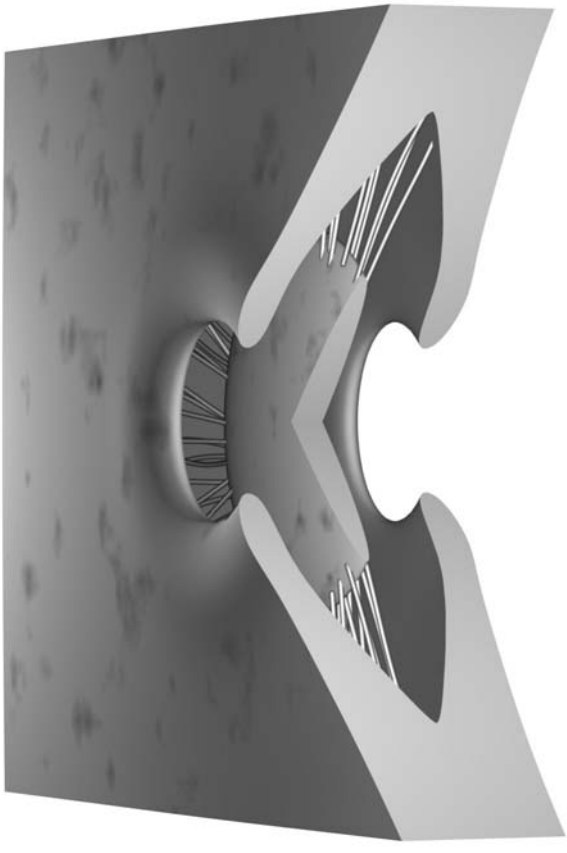

Fig. 2. A schematic 3D image of a bordered pit. A sector has been cut out of the pit chamber in order to make the inner structure of the pit visible. The impermeable disc in the middle of the pit chamber is the torus, which is suspended by the, in reality, complex network of microfibrillar strands, the margo. The pit apertures form the inlet and the outlet for the sap flow through the pit. Visualization by Jyrki Hokkanen, Center for Scientific Computing (Finland).

include fluid flow in porous medium,[9, 10] suspension flows,[11, 12] and multiphase flows.[13–15] The key idea behind this method is to solve a discretized Boltzmann equation for particle distributions on a regular lattice. At each time step the particles first propagate to the neighboring lattice points and then interact through local collisions in which their momenta are redistributed. Hydrodynamical variables like density ρ and velocity $\mathbf{u}$ are obtained from the velocity moments of the distribution function f_i.

Fig. 3. A TEM replica of the fibrillar structure of a sapwood pit of *Tsuga canadensis*. The diameter of the margo is 18 μm and the largest diameter of the torus (T) is 9 μm. Openings in the margo are up to 1 μm wide in the circumferential direction and up to 2 μm wide in the radial direction. Courtesy of Springer-Verlag.[29]

In Section 2 below we give a brief introduction to the lattice-Boltzmann method used here, and in Section 3 discuss how continuum porous media can be included in the lattice-Boltzmann simulations, and present some benchmark studies on this topic. Next, in Section 4, we show our simulation results for fluid flow through random screens that we have used to model the margo. Then, in Section 5, we present our simulation results for sap flow through a bordered pit of conifer xylem. Finally, in Section 6, we discuss the simulation results, and draw some conclusions.

2. THE LATTICE-BOLTZMANN METHOD

There are several different lattice-Boltzmann models available. In this work we have used the so-called lattice-BGK model, which is the simplest one in the hierarchy of lattice-Boltzmann methods. The dynamics of this model is given by the equation[3, 5, 6]

$$f_i(\mathbf{r}+\mathbf{c}_i, t+1) = f_i(\mathbf{r}, t) + \frac{1}{\tau}\left(f_i^{\mathrm{eq}}(\mathbf{r}, t) - f_i(\mathbf{r}, t)\right) \tag{1}$$

where $\mathbf{c}_i$ is a vector pointing to a neighboring lattice node, $f_i(\mathbf{r}, t)$ is the density of the particles moving in the $\mathbf{c}_i$-direction, τ is the BGK relaxation parameter, and $f_i^{\text{eq}}(\mathbf{r}, t)$ is the equilibrium distribution towards which the particle populations are relaxed. The equilibrium distribution can be chosen in different ways. A common choice is

$$f_i^{\text{eq}} = t_i \rho \left[1 + \frac{1}{c_s^2} (\mathbf{c}_i \cdot \mathbf{u}) + \frac{1}{2c_s^4} (\mathbf{c}_i \cdot \mathbf{u})^2 - \frac{1}{2c_s^2} u^2 \right] \tag{2}$$

in which t_i is a weight factor depending on the length of the link vector $\mathbf{c}_i$, and c_s is the speed of sound in the fluid. The weights t_i can also be chosen in several ways. In our simulations they have been chosen as $\frac{1}{3}$, $\frac{1}{18}$ and $\frac{1}{36}$ for the rest particle and the particles moving to the nearest and next nearest neighbors, respectively. The speed of sound for this model and the kinematic viscosity of the simulated fluid are $c_s = \frac{1}{\sqrt{3}}$ and $\nu = \frac{2\tau - 1}{6}$, respectively. The hydrodynamic density ρ and velocity $\mathbf{u}$ are obtained as moments of the distribution function f,

$$\rho(\mathbf{r}, t) = \sum_i f_i(\mathbf{r}, t) \tag{3}$$

and

$$\rho(\mathbf{r}, t)\, \mathbf{u}(\mathbf{r}, t) = \sum_i \mathbf{c}_i f_i(\mathbf{r}, t) \tag{4}$$

(Here and below lattice units are always used, if the units are not specified.) The fluid pressure is given by

$$p(\mathbf{r}, t) = c_s^2 \rho(\mathbf{r}, t) \tag{5}$$

Notice that, when systems with a very small Reynolds number are simulated, the nonlinear Navier–Stokes equation can be replaced with the linear Stokes equation. In the lattice-Boltzmann model this is accomplished by removing the two nonlinear terms in the equilibrium distribution function Eq. (2).

The physical boundary condition at solid-fluid interfaces is the no-slip condition, i.e., the fluid adjacent to the solid surface moves with the velocity of the surface. In lattice-Boltzmann simulations, the no-slip boundary condition is usually realized using the so-called bounce-back condition.[16–18] In this approach the momenta of the particles meeting the solid walls are simply reversed. The no-slip boundary is located somewhere between the last fluid point and the first wall point, the exact place of the no-slip

boundary depending on the relaxation parameter τ and the geometry of the system.[17, 18] For practical simulations the bounce-back boundary is very attractive because it is simple and computationally efficient.

Successful numerical simulation of practical fluid-flow problems requires that the velocity and pressure boundary conditions of the system have been imposed in a consistent way. General velocity and pressure boundaries are still being developed for the lattice-Boltzmann method. So far most of the practical simulations have used a body force[9, 17, 19] instead of pressure or velocity boundaries. When a body force is used, a pressure gradient acting on the fluid is replaced by a uniform external force that gives acceleration g to the fluid. Pressure fields are obtained from the effective pressure p_{eff}, defined as

$$p_{\text{eff}}(\mathbf{r}, t) = c_s^2(\rho(\mathbf{r}, t) - \bar{\rho}) - \bar{\rho} g x \tag{6}$$

in which $\bar{\rho}$ is the mean density of the fluid and x is the distance in the flow direction from the inlet of the system. Usually periodic boundaries are imposed in the direction of the flow. Conditions that are very close to pressure boundaries can be obtained by averaging the velocity and pressure fields over the planes of the inlet and the outlet of the simulated system.[17]

3. LATTICE-BOLTZMANN MODELS FOR CONTINUUM POROUS MEDIA

In setting up a complex flow problem for simulation, it may be desirable to include in the simulation a region whose detailed geometry cannot be resolved in full detail. A common approach then is to treat such a region as a porous medium, whose properties are defined such as to model the true effect of the region on the overall flow. This kind of macroscopic modeling is useful in many large-scale problems such as flow through heat exchangers and radiators, as well as in smaller-scale problems such as flow in fibrous materials.[20, 21]

Single-fluid flows in rigid and isotropic porous media usually obey Darcy's law,[22]

$$\mathbf{q} = -\frac{k}{\mu} \nabla p \tag{7}$$

where $\mathbf{q}$ is the volumetric fluid flux through the medium, μ is the dynamic viscosity of the fluid, p is the fluid pressure, and k is the permeability coefficient that is a measure for fluid conductivity of the medium. (For heterogeneous porous media $k = k(\mathbf{r})$.) The volumetric flow can also be

written as $\mathbf{q} = \phi\mathbf{v}$, where ϕ is the porosity of the medium, and $\mathbf{v}$ is the average velocity of the fluid inside the medium. If the medium is anisotropic, the permeability k of the medium must be replaced by a permeability tensor $\bar{\mathbf{K}}$, and the Darcy's law can be expressed in the form[22]

$$\mathbf{q} = -\frac{\bar{\mathbf{K}} \cdot \nabla p}{\mu} \tag{8}$$

Equations (7) and (8) have been found to work very well for a wide variety of natural and artificial porous media when the fluid velocity is small. With high velocities, however, nonlinear effects become important, and these equations are no more applicable. These equations also suggest that the original porous medium can often be replaced in simulations with a continuum medium that has the same permeability.

A standard treatment of stationary creeping-flow problems in which there appear a combination of open and porous regions, involves application of the Stokes and Brinkman equations.[20] Fluid flow in the open regions is governed by the Stokes equation,

$$\mu\nabla^2\mathbf{u} = \nabla p \tag{9}$$

while inside the porous medium the flow is modeled by the Brinkman equation,

$$\mu\nabla^2\mathbf{q} - \frac{\mu}{k}\mathbf{q} = \nabla p \tag{10}$$

(We assume here an isotropic porous medium.)

Several lattice-Boltzmann models have been developed for isotropic porous media, which obey Darcy's law Eq. (7).[20, 21, 23, 24] Here we will only discuss the model of ref. 20, which we also use in our simulations. In this model the Brinkman equation is recovered by modifying the standard equilibrium distribution Eq. (2) such that the magnitude of the momentum is reduced, while the direction of the momentum is left unchanged. This can be accomplished by changing the velocity $\mathbf{u}(\mathbf{r}, t)$ in the equilibrium distribution Eq. (1) such that it becomes[20]

$$\mathbf{U}(\mathbf{r}, t) = \mathbf{u}(\mathbf{r}, t) + \frac{\tau\mathbf{F}(\mathbf{r}, t)}{\rho(\mathbf{r}, t)} \tag{11}$$

where ρ is the fluid density, and τ is the relaxation parameter defined in Eq. (1). The Brinkman equation is then recovered with the choice

$$\mathbf{F}(\mathbf{r}, t) = -\beta\rho(\mathbf{r}, t)\,\mathbf{u}(\mathbf{r}, t) \tag{12}$$

where β is a resistance parameter. Notice that substitution of Eq. (12) to Eq. (11) gives

$$\mathbf{U}(\mathbf{r}, t) = (1-\beta\tau)\,\mathbf{u}(\mathbf{r}, t) \tag{13}$$

i.e., this choice for $\mathbf{F}(\mathbf{r}, t)$ amounts to rescaling of the fluid velocity.

Now, for small values of β, the permeability k of the modeled medium is approximately given by[20]

$$k \approx \frac{\mu}{\rho\beta} \tag{14}$$

This result Eq. (14) is, however, inaccurate for high values of β. The correct permeability is[21]

$$k = \frac{(2-\beta)\,\mu}{2\beta\rho} \tag{15}$$

This equation can be written in the form

$$k = \frac{\mu}{\rho\beta^*} \tag{16}$$

where the "effective" resistance parameter β^* is defined by

$$\beta^* = 2\beta/(2-\beta) \tag{17}$$

Notice that parameter β and thus permeability k can be made dependent on position $\mathbf{r}$. The method can thus be used to simulate both homogeneous and heterogeneous porous media.

We have performed benchmark studies for Stokes flow through a porous plate located in the middle of a rectangular tube. The length to width ratio of the tube is 3, and periodic boundary conditions are imposed in the direction of the flow. A body force is used, and the relaxation parameter is set to $\tau = 1.0$ in all simulations.

For Stokes flow the pressure drop Δp in the tube can be written in the form

$$\Delta p = \frac{C}{\mathrm{Re}} \times \frac{1}{2}\rho U^2 \tag{18}$$

Here $\mathrm{Re} = \rho\ell U/\mu$ is the tube Reynolds number, ℓ is the side length of the square cross section, U is the average fluid velocity, and C is a (dimensionless) pressure drop coefficient.

Table I. Dimensionless Pressure Drop Coefficient $C_{\text{tube}} = \Delta p\, \text{Re}/\frac{1}{2}\rho U^2$ for a Rectangular Tube. The Length to Width Ratio of the Tube Is 3. l Is the Side Length of the Cross Section, and $\Delta\%$ Shows the Relative Difference in C_{tube} when Compared to the Result in the Continuum Limit

ℓ	C_{tube}	$\Delta\%$
10	162.6	4.7
20	168.6	1.2
30	169.8	0.5
40	170.2	0.3
80	170.6	0.1
∞	170.7	

In Table I we show the simulated pressure drop coefficients C_{tube} for tubes without a porous plate for five different resolutions. The results fall on a straight line when plotted as a function of $1/\ell^2$, as also they should because the lattice-Boltzmann method is spatially second-order convergent.[17, 25] The value 170.7 for the dimensionless pressure drop coefficient, obtained by extrapolating the simulation results (see Table I) to the continuum limit, is up to four digits exactly the same as that obtained by summing the analytical series expansion for the square tube.[26]

In Table II, results for the tubes with a porous plate are presented. Two different plates were used. The β values for the porous plates were chosen with the help of Eq. (15) so that the dimensionless permeabilities k/ℓ^2 were equal for all tube sizes. This way the tubes of different ℓ can be interpreted to represent the same system with different lattice resolutions. It is evident from Table II that the relative increase in the pressure drop due

Table II. Scaled Pressure Drop Coefficients c for Geometrically Identical Rectangular Tubes with a Porous Plate; β^* Is the "Effective" Resistance Parameter of Eq. (16), h Is the Thickness of the Porous Plate, and $c = C/C_{\text{tube}}$ with C_{tube} the Pressure Drop Coefficient Without the Porous Plate

ℓ	β^*	h	c	β^*	h	c
10	0.100	1	1.091	1.00	1	1.803
20	0.0250	2	1.094	0.250	2	1.845
30	0.0111	3	1.094	0.111	3	1.854
40	0.00625	4	1.095	0.0625	4	1.858
80	0.00156	8	1.095	0.0156	8	1.862

Table III. Dimensionless Pressure Drop Coefficients *C* for a Rectangular Tube with *l* = 40, when the Thickness *h* of the Porous Plate Is Varied Such that *h*/*k* Is Kept Constant

β^*	h	C	β^*	h	C
0.025	1	186.2	0.25	1	315.2
0.0125	2	186.3	0.125	2	315.5
0.00833	3	186.3	0.0833	3	315.8
0.0625	4	186.3	0.625	4	316.2

to the porous plate is almost independent of the lattice resolution. Finally, in Table III, we compare for $\ell = 40$ the pressure drop for different plate thicknesses h when h/k is kept constant. It is clear that the pressure drops are practically independent of h. The thickness of the simulated porous object can thus be quite small, even one lattice spacing can sometimes be sufficient.

4. SIMULATIONS OF FLUID FLOW THROUGH RANDOM SCREENS

Fluid flow through screens and wire gauzes is a problem that has several applications such as, e.g., reduction of turbulence in wind tunnel experiments.[27] There are also many biological systems which involve fluid flow through thin net like structures. Small flying insects, e.g., have wings that are composed of minute open-grid structures.[28] Also, sap flow between the neighboring tracheids in conifer xylem passes through pits which include a very complicated net like structure of microfibrillar strands. Typical electron micrograph of the structure is shown, e.g., in ref. 29 (see Fig. 3).

In industrial applications the screens are usually regular and the flow velocities are rather high. For this reason previous studies have usually concentrated on regular screens and on moderate or large Reynolds numbers.[27, 31, 32] There is very little information available about the pressure drop through screens in the low Reynolds-number regime.[33] However, in many biological systems the structures are irregular, and, due to the microscopic nature of these systems, the Reynolds numbers are often very small.

The pressure drop Δp for Stokes flow through a wire screen can be written in the form[33]

$$\Delta p = G(\alpha) \frac{C'}{\mathrm{Re}} \times \frac{1}{2} \rho U^2 \tag{19}$$

where U is the upstream velocity of the fluid, ρ is the fluid density, and $\mathrm{Re} = \rho\, dU/\mu$ is the Reynolds number with d the diameter of the fibers. The dependence of the dimensionless pressure drop coefficient C (see Eq. (18)) on the screen porosity α (the fraction of unblocked area of the gauze) is written here explicitly as

$$C = G(\alpha)\, C' \tag{20}$$

Here $G(\alpha)$ is a function that depends on the structure and porosity α of the screen, and C' is a constant. The "porosity function" $G(\alpha)$ and the constant C' are difficult to obtain analytically. Most of the previous work has thus been based on experimental correlations, and there are several suggestions as to the functional form of $G(\alpha)$. A good review on this topic for regular woven screens is given in ref. 34.

We have performed direct numerical simulations of Stokes flow through both regular and random screens.[35] In these simulations the flow direction was perpendicular to the screen, the relaxation parameter was set to $\tau = 1.0$ and a body force was used. On both sides of the screen an open layer of fluid of thickness W was added, periodic boundaries were imposed in all directions, and the density and momentum of the fluid were averaged over the inlet and outlet planes of the system. In this way conditions that are very close to pressure boundaries can be obtained.[17]

The irregular screens were constructed of cylinders with a diameter to length ratio of 1:20. The cylinders were placed randomly on a planar substrate, and they were freely overlapping and randomly oriented. Periodic boundary conditions were imposed at the boundaries (See Fig. 4).

In order to find an acceptable grid resolution, we did several test runs for random screens using fiber diameters $d = 10$ and $d = 20$. For screen porosities $\alpha = 0.30$ and 0.50, e.g., the respective pressure drop coefficients C were 7 and 2% smaller for the systems with the finer discretization. Thus, as the convergence of the present method is approximately second order in space, i.e., the deviation from the exact value is proportional to the square of the grid spacing, we could deduce that for $d = 10$ the discretization errors were about 10 and 3% for $\alpha = 0.30$ and 0.50, respectively.

Corresponding simulations for regular screens (see ref. 35 for details) gave much smaller errors. For the discretization levels used above, the differences between the simulated pressure drop coefficients were found to be always less than 0.1% when the screen porosity α was greater than 0.2. Difference between the regular and irregular screens can be explained by the rather abundant small holes found in random screens, which are very sensitive to discretization effects (see Fig. 4). The relative number of small holes decreases when the screen porosity increases, and hence the effect of

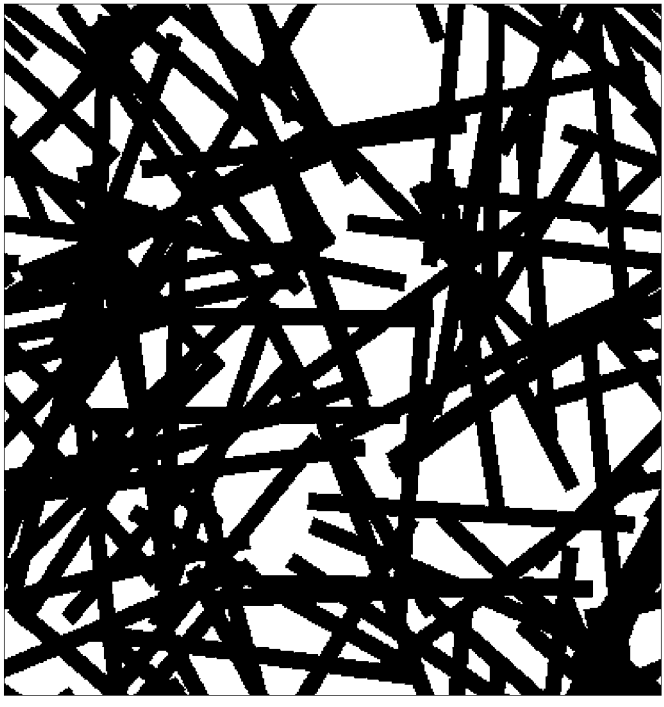

Fig. 4. A random fiber screen with screen porosity $\alpha = 0.328$.

discretization also decreases. In regular screens this kind of effect does not appear.

The simulated pressure drops are also quite sensitive to the thickness W of the open fluid layer on both sides of the screen, especially for high screen porosities. The dimensionless pressure drop C tends to decrease when W is increased. We found that the error was smaller than 7% if W/d was chosen to be larger than 15.[35]

The actual simulations were performed for $d = 10$, while W/d varied between 15 and 20 depending on the screen porosity. Here we had to compromise between the lattice dimensions and the number of time steps used in the iterations because of limitations in the computer resources. More time steps were needed when the screen porosity was high. The total numerical errors in the pressure drops determined were estimated to be less than 10% in all cases.[35] The variation in the pressure drop coefficients C for different screen realizations of equal porosity was found to be about 15% (cf. Fig. 5).

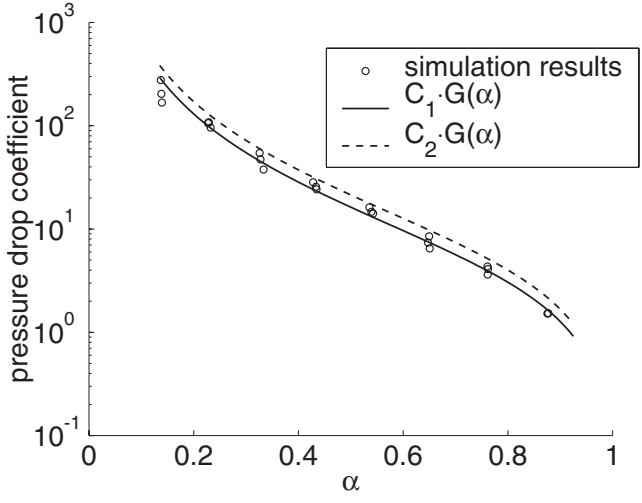

Fig. 5. The simulated pressure drop coefficients for random fiber screens (o). The curve fitted to the simulation data is $C_1G(\alpha)$, where $C_1 = 5.4$, and $G(\alpha) = (1-\alpha^2)/\alpha^2$. The dependence of pressure drop on screen porosity, in the form $C_2G(\alpha)$ with $C_2 = 7.125$, as given by ref. 36 in the low Reynolds-number limit for the data on regular woven screens,[33] is shown for comparison.

The simulation results for random screens are presented in Fig. 5. The best fit to the dimensionless pressure drop coefficients C as a function of screen porosity α was obtained when the screen porosity function was chosen as

$$G(\alpha) = \frac{1-\alpha^2}{\alpha^2} \tag{21}$$

The value of parameter C' that gave the best fit for this function $G(\alpha)$ was 5.4. A general formula for the pressure drop in regular woven screens is given in ref. 36. In the low Reynolds number limit the dominant term of this formula is similar to the one shown in Eq. (19), with $C' = 7.125$ and $G(\alpha)$ given by Eq. (21). The flow resistances of the random fiber screens are thus somewhat lower than those of regular woven screens (see also Fig. 5). This is because the void size distribution has a detectable effect on the pressure drop as the biggest voids dominate the flow. In regular screens all voids are identical whereas in random screens the void-size distribution is fairly wide. Notice that this effect is also seen with thick fiber webs for which randomness is known to decrease the pressure drop by up to 30–40%.[10]

5. SIMULATIONS OF WATER FLOW THROUGH BORDERED PITS OF CONIFER XYLEM

In this Section, we present preliminary numerical results for the pressure drop in sap flow through pits of conifer xylem. The geometrical properties of the simulated pit were here determined from a few electron micrographs, and no effort to include realistic variations in the structure was made. A more thorough analysis of this problem can be found in ref. 37. The data of ref. 35 were utilized to estimate the total hydrodynamical pressure drops that take place in sap flow in living conifers.[37]

A typical cross section of a pit is shown in Fig. 6. The neighboring cell lumens are situated to the left and to the right of the image, and the sap is flowing through the pit via the aperture around the practically impermeable circular torus in the middle of the pit chamber. The torus is suspended by a thin net-like structure, the margo, which can be seen in Fig. 3.

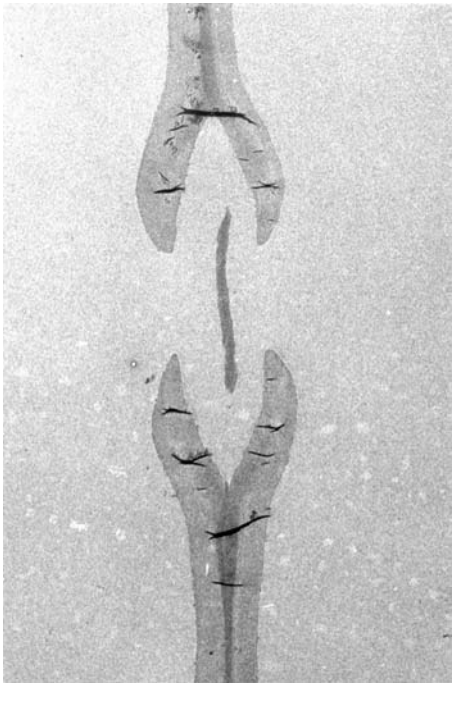

Fig. 6. An earlywood bordered pit pair of Scots pine. The torus can be seen in the middle of the pit chamber. The margo, through which the torus is attached to the edge of the pit chamber, is not visible in this replica. Courtesy of Pekka Saranpää, The Finnish Forest Research Institute, METLA.

In principle sap flow simulations could be performed for true 3D tomographic images of the pits. Such images are not, unfortunately, available. For this reason a model for the pit is needed. The geometry of the pit is known to be approximately axially symmetric, and a three-dimensional model of the pit can be made by rotating the cross sectional image (Fig. 6) around its symmetry axis (Fig. 2).

The margo is a very complicated structure and cannot be digitized finely enough because the pit would then require three-dimensional lattices too large for practical simulations. The frictional effect of the margo can however be taken into account in the flow simulations by replacing it with a continuum porous plate. A homogeneous model used for the margo should not cause large effects on the flow in the scale of the whole pit, and the errors due to this simplification should thus be rather small.

The pit-flow simulation conditions were similar to those in the random screen simulations: body force was imposed, the relaxation parameter was $\tau = 1.0$, an open fluid layer of thickness W was added on both sides of the pit, periodic boundaries where imposed in all directions, and velocity and pressure fields were averaged over the inlet and outlet planes of the simulation box. Actually, due to the periodicity, the model system consists of pits that are repeated periodically in the pit plane, forming thus a kind of porous plate. On real cell walls the pits are quite close to one another. For this reason we have chosen the simulation box only slightly bigger than the inner diameter of the pit. In ref. 37 the dependence of the pressure drop on the packing density of the pits is studied in detail.

The total pressure drop Δp_{tot} between the two sides of the pit can be written in the same form as that in Eqs. (18) and (19), namely $\Delta p_{\text{tot}} = \frac{C}{\text{Re}} \times \frac{1}{2} \rho U^2$, where U is the upstream velocity of the fluid. The Reynolds number is now $\text{Re} = \rho a U / \mu$, where a is the diameter of the pit aperture. The total pressure drop Δp_{tot} consists of three ingredients, the inflow pressure drop Δp_i, the actual pit pressure drop Δp_p and the outflow pressure drop Δp_o. (The pit pressure drop Δp_p is defined as the pressure difference between the inlet and the outlet of the pit.) Due to the approximate symmetry, and the Stokes-flow assumption, $\Delta p_i \approx \Delta p_o$.

The simulations below show that, with the packing density of the pits used here, the pressure drop Δp_p dominates the total pressure drop.

The simulations were first performed without the margo. The image shown in Fig. 6 was discretized with several grid spacings in order to find the sufficient lattice size. Different thicknesses W of the open fluid layer were also tested. We found that the results for the pressure drop coefficient were precise enough when, in the direction of the flow, the dimension of the simulation volume was roughly equal to the diameter of the pit chamber (see Fig. 7). Therefore the simulation volumes, just large enough

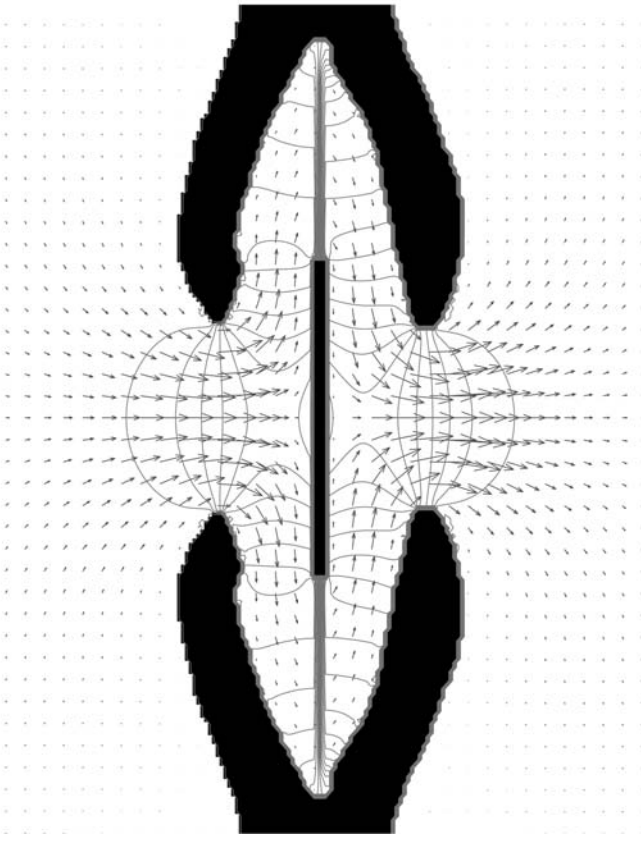

Fig. 7. An axial cut of the 3D pressure and velocity fields of fluid flow through a bordered pit. The margo was described as a homogeneous plate with an appropriate resistance coefficient.

to enclose the pit, were taken to be cubic. This choice can be justified by examining the pressure and velocity fields in Fig. 7, where for the linear size of the cube $L = 200$ was used. The simulation volume was large enough to contain all the pressure contours, i.e., the inflow and outflow pressure losses were negligible.

Five different grids were tested such that L ranged from 200 to 440 lattice units. The pressure drop coefficients defined in Eq. (18) were calculated from the simulation results. It is evident from Fig. 8 that $L = 360$ is sufficient for an error less than 5%, which is good enough with respect to the other sources of error.

The screen porosity α of the margo can be obtained by estimating, via image analysis, the percentages of white and black areas in Fig. 3. It is also

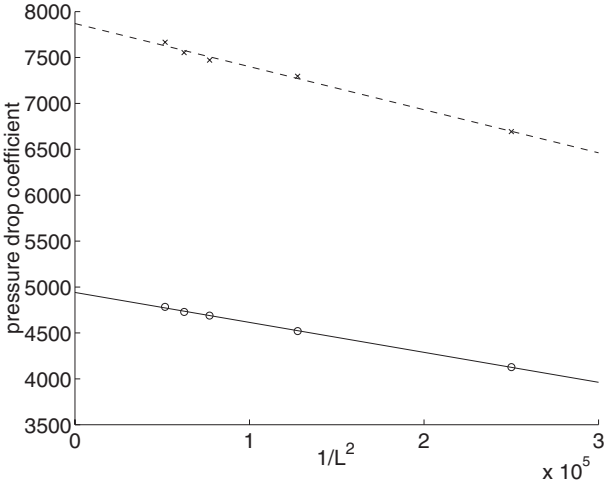

Fig. 8. Dimensionless pressure drop coefficients C for the pit shown in Fig. 6, with and without the margo. The values appear to depend linearly on $1/L^2$ (the method is second order convergent).

evident from the Fig. 3 that α can be taken independent of the angular position. We have also neglected the radial variation in α and used for it the averaged value $\alpha = 0.44$. When all the fibers are assumed to be circular with a constant diameter d, the permeability k of the continuum plate replacing the margo can be estimated from the random screen results presented in the previous section. The margo can then effectively be replaced in the simulations by a homogeneous medium having an appropriate resistance parameter β.

If the values of permeability, as determined from Eqs. (7) and (16), are set equal, and the "effective" resistance parameter β^* is solved, we get

$$\beta^* = \frac{\Delta p}{\rho q h} \tag{22}$$

where the gradient ∇p has been replaced by the pressure drop Δp divided by the thickness h of the layer over which the pressure drop occurs. If the pressure drop Δp of Eq. (19) is substituted in Eq. (22), and the volumetric flux q is set equal to the upstream velocity U, we find that

$$\beta^* = C' G(\alpha) \times \frac{U}{2h\mathrm{Re}} \tag{23}$$

Here Re is the Reynolds number defined as $\mathrm{Re} = \rho\, dU/\mu$, where d is the diameter of the fibers. When this definition of Reynolds number is substituted in Eq. (23), we find furthermore that

$$\beta^* = C'G(\alpha) \times \frac{v}{2hd} \tag{24}$$

in which $v = \mu/\rho$ is the kinematic viscosity of the fluid. The thickness of the margo, estimated from an electron microscope image, is approximately 0.1 μm. The inner diameter of the pit chamber, estimated from Fig. 6, is about 17 μm. If the length of the simulation cube L is chosen to be 20 μm, the thickness of margo is then $L/200$ lattice units. This value was used for diameter d in the expression for the Reynolds number. In principle the value of h, the distance over which the pressure drop in the margo occurs, should be about the same as the diameter d. However, as we take h to be the thickness of the permeable layer in lattice units, it has to be an integer. Therefore h cannot be exactly the same as d, which takes different real values depending on L. However, our simulations with the square tubes (see Table III) and pits (data not shown) show that the exact value of h is not important as long as the product $\beta^* h$ is kept constant. According to Eq. (24), β^* is inversely proportional to h so that this condition is automatically satisfied, and the value of h can be chosen accordingly. A natural choice is usually the integer nearest to d.

The value of β^* can be calculated from Eqs. (21) and (24). If, for example, the size of the simulation volume is $L = 200$, then $d = L/200 = 1$, and if h is taken to be equal to 1, the value of β^* is

$$\beta^* = 5.4 \times \frac{(1-0.44^2)/0.44^2 \cdot 1/6}{2 \cdot 1 \cdot 1} \approx 1.9 \tag{25}$$

The parameter β that appears in Eq. (12) can now be solved from Eq. (17), and the result is $\beta \approx 0.97$. This parameter is then used in flow simulations.

In Fig. 7 we show the pressure contours and the velocity field visualizing the results of a pit simulation. The pressure difference between the adjacent contours is constant. There are 41 contours in Fig. 7, of which 5 reside in each of the pit openings, corresponding to about 25% of total pressure drop when put together. The relative contribution of the margo and the rest of the pit chamber cannot be resolved by simply counting the contours. The margo changes the flow pattern so that it becomes more uniform in its vicinity. Since Stokes flow is assumed, the pressure drop at each point of the margo is proportional to the flow velocity at that point. Because of the linear dependence, the total pressure drop over the margo can be estimated

using the average fluid velocity at that point, which is easy to do from the simulated velocity field. The result is that about 25% of the total pressure drop is due to the margo. The contribution of the rest of the pit chamber is thus about 50%.

Another way to estimate the effect of margo is to run the simulations for identical pits with and without the margo. This was done with a series of different discretizations (see Fig. 8). For example, the results for C, corresponding to the discretization level used in Fig. 7, were 4128 and 6693 without and with the margo, respectively. We can deduce that the part of the total pressure drop that is due to having the margo in the system is about 38%. This percentage is clearly larger than the 25% obtained by direct calculation. The explanation to this difference is obviously the fact that the presence of the margo alters the flow pattern so that it becomes more plug-like, which considerably increases also the viscous friction on the walls of the pit chamber. Hence part of the increase in flow resistance is not due to the margo itself but to the increased viscous friction resulting from the changed velocity field. A more detailed analysis of wall stresses and pressure fields is obviously needed for a full account of this effect.

In ref. 38 the relative contributions to the flow resistance of different parts of the pit structure have been estimated. There a model was used in which the flow volume was divided into parts that were approximately regular in shape. Then known results for the resistances of these geometrical shapes were applied. All parts could not be treated this way because of the complexity of the shapes. These parts were simply neglected in the model. The resistance of the pit apertures and of the pores in the margo were approximated by the Hagen–Poisseuille equation, which obviously is a crude approximation. Also, it was not properly explained how the estimations were made, and what assumptions were made, e.g., of the pores in the margo. One component of the total resistance in the estimation was the resistance of the cell lumen which we have not studied here. If the contribution of the lumen is separated, the contributions of the margo and the pit apertures can be compared with our results. The calculations in ref. 38 were made for Scots pine (*Pinus sylvestris L.*) both for the earlywood and the center of latewood (our model is based on earlywood images). The results are presented as curves that illustrate the relative contributions of the parts of the flow path to the total resistance as a function of pressure difference across a single tracheid. When the pressure difference is large, the system cannot be considered rigid, and the deflection of the torus towards the pit border should be taken into account. Our results should be compared to those which describe the case of low pressure differences because we do not take the deflection into account. The results estimated from the curves (the effect of the lumen excluded) show that, in latewood,

the contribution of the margo in comparison with that of the pit apertures is roughly tenfold.

On the other hand, in earlywood the contribution of the pit apertures seems to be negligible (this cannot be reliably read from the curve). The simulations in our case show that the contribution of the margo is of the same magnitude as the contributions of the pit apertures. A probable explanation to this difference is that the margos used in ref. 38 were much more encrusted having thicker strands and much smaller voids than the one used in our simulations. Our simulations of random fiber screens (Fig. 5) show that the screen porosity is a very sensitive parameter in the flow resistance of screens. The margo we use in our simulations (Fig. 3) looks much more permeable than those shown in ref. 38, and it is therefore understandable that its contribution to the pressure loss is thus considerably smaller.

6. CONCLUSIONS

We have used the lattice-Boltzmann method to simulate fluid flow through screens of random fibers, and found an explicit form for the pressure drop coefficient as a function of screen porosity. Also, we used a similar method to simulate flow through a layer of homogeneous medium. By comparing the pressure drop over the homogeneous layer with that resulting from the simulations for random fiber screens, we were able to replace the screen by an effective homogeneous plate in the large-scale simulations.

As an application we studied sap flow through a typical bordered pit of a conifer. These pits involve a net like structure, the margo, which was modeled as a homogeneous plate with the same flow resistance as the margo. There are however unresolved uncertainties as for the practical applicability of the simulation results. There is a large natural variability in the wood structure, and pit shapes vary appreciably even within the same species of conifer, depending, e.g., on the time of growth of the tracheid. Even more important seems to be the variability in the margo, of which detailed information was not available. Our present simulations should thus be regarded as a case study, and as a demonstration of the potential of the lattice-Boltzmann method for complicated flow problems in biological systems.

In addition to neglecting the natural variability in the wood structure, the pit was assumed to be axially symmetric. This approximation can be assumed to be quite reasonable as the pits generally appear to be quite symmetric. A similar assumption was that the margo was composed of fibrils with a fixed circular cross section, all lying in the same plane, and

that the screen porosity of the margo is homogeneously distributed. The last assumption can be relaxed, and the true distribution of screen porosity can be included in the simulations. Also, we neglected the displacement of the torus towards the pit borders on the downflow side,[39] as simulations were restricted to the creeping flow regime. In spite of these assumptions, we believe that the results we report here provide a qualitatively correct description of sap flow through pits in the tracheids of conifer xylem.

As already explained above, the structural properties of pits between conifer tracheids vary appreciably, and this variability has a noticeable effect on flow resistance. Also the locations and numbers of pits vary in tracheids. The effects on permeability of these variations will be reported in a forthcoming publication. We plan as well to model a whole tracheid, and the xylem structure composed of these tracheids, in which flow will then be simulated. Our ambition is to eventually obtain by flow simulations a better understanding of the permeability of tracheids, a quantity that is not easy to study experimentally on the cellular scale.

ACKNOWLEDGMENTS

Financial support from the Technology Development Centre (Finland), and the Academy of Finland (projects No. 44875 and 47811), is gratefully acknowledged. We are also grateful to Urpo Aaltosalmi for preparing the data related to the geometry of the random networks of fibers, and to Jyrki Hokkanen for the visualization of Fig. 2.

REFERENCES

1. W. F. Pickard, *Prog. Biophys. Molec. Biol.* **37**:181 (1981).
2. M. Borghetti, J. Grace, and A. Raschi, eds., *Water Transport in Plants under Climatic Stress* (Cambridge University Press, New York, 1993).
3. R. Benzi, S. Succi, and M. Vergassola, *Phys. Rep.* **222**:145 (1992).
4. Y. H. Qian, D. d'Humiéres, and P. Lallemand, *Europhys. Lett.* **17**:479 (1992).
5. D. H. Rothman and S. Zaleski, *Lattice-Gas Cellular Automata* (Cambridge University Press, Cambridge, 1997).
6. B. Chopard and M. Droz, *Cellular Automata Modelling of Physical Systems* (Cambridge University Press, Cambridge, 1998).
7. U. Frisch, B. Hasslacher, and Y. Pomeau, *Phys. Rev. Lett.* **56**:1505 (1986).
8. U. Frisch, D. d'Humiéres, B. Hasslacher, P. Lallemand, Y. Pomeau, and J.-P. Rivet, *Complex Syst.* **1**:649 (1987).
9. B. Ferréol and D. H. Rothman, *Transport in Porous Media* **20**:3 (1995).
10. A. Koponen, D. Kandhai, E. Hellén, M. Alava, A. Hoekstra, M. Kataja, K. Niskanen, P. Sloot, and J. Timonen, *Phys. Rev. Lett.* **80**:716 (1998).
11. A. J. C. Ladd, *J. Fluid Mech.* **271**:285 (1994); *ibid.* **271**:311 (1994).

12. P. Raiskinmäki, A. Shakib-Manesh, A. Koponen, A. Jäsberg, M. Kataja, and J. Timonen, *Comp. Phys. Comm.* **129**:185 (2000).
13. X. Shan and H. Chen, *Phys. Rev. E* **49**:2941 (1994).
14. N. S. Martys and H. Chen, *Phys. Rev. E* **53**:743 (1996).
15. P. Raiskinmäki, A. Koponen, J. Merikoski, and J. Timonen, *Comp. Mat. Science* **18**:7 (2000).
16. M. Gallivan, D. Noble, J. Georgiadis, and R. Bockius, *Int. J. Numer. Meth. Fluids* **25**:249 (1997).
17. D. Kandhai, A. Koponen, A. Hoekstra, M. Kataja, J. Timonen, and P. Sloot, *J. Comp. Phys.* **150**:482 (1999).
18. X. He, Q. Zou, L. Luo, and M. Dembo, *J. Stat. Phys.* **129**:357 (1996).
19. J. Buick and C. Greated, *Phys. Rev. E* **61**:5307 (2000).
20. M. Spaid and F. Phelan, Jr., *Phys. Fluids* **9**:2468 (1997).
21. D. M. Freed, *J. Mod. Phys. C* **9**:1491 (1998).
22. A. Scheidegger, *The Physics of Flow in Porous Media* (Macmillan, New York, 1957).
23. O. Dartis and J. McCloskey, *Phys. Rev. E* **57**:4834 (1998).
24. O. Dartis and J. McCloskey, *Geophys. Res. Lett.* **25**:1471 (1998).
25. R. Maier, R. Bernard, and D. Grunau, *Phys. Fluids* **8**:1738 (1996).
26. F. M. White, *Viscous Fluid Flow* (McGraw-Hill, Singapore, 1991).
27. J. Groth and A. V. Johansson, *J. Fluid Mech.* **197**:139 (1988).
28. A. M. Kueth, *Swimming and Flying in Nature* **2**:806 (1975).
29. G. L. Comstock and W. A. Côté, *Wood Science and Technology* **2**:279 (1968).
30. B. A. Meyland and B. G. Butterfield, *Three-Dimensional Structure of Wood* (Chapman and Hall, London, 1971).
31. W. J. D. Annand, *J. Royal Aeron. Soc.* **57**:141 (1953).
32. K. E. G. Wieghart, *The Aeronautical Quarterly* **4**:186 (1953).
33. B. R. Munson, *J. Fluid Eng.* **110**:462 (1988).
34. R. A. Pinker and M. V. Herbert, *J. Mech. Eng. Sci.* **9**:11 (1967).
35. A. Valli, A. Koponen, and J. Timonen, to be published.
36. E. Brundrett, *J. Fluid Eng.* **115**:293 (1993).
37. A. Valli, A. Koponen, T. Vesala, and J. Timonen, to be published.
38. A. J. Bolton, *Leiden Botan. Series* **3**:222 (1976).
39. S. C. Gregory and J. A. Petty, *J. Exp. Bot.* **24**:763 (1973).